

“RED” BUT NOT “DEAD”: ACTIVELY STAR-FORMING BRIGHTEST CLUSTER GALAXIES AT LOW REDSHIFTS

JAMES RUNGE[†] AND HAOJING YAN[‡]

Department of Physics and Astronomy, University of Missouri - Columbia

Draft version July 1, 2021

ABSTRACT

Brightest Cluster Galaxies (BCGs) are believed to have assembled most of their stars early in time and, therefore, should be passively evolving at low redshifts and appear “red-and-dead.” However, there have been reports that a minority of low-redshift BCGs still have ongoing star formation rates (SFR) of a few to even $\sim 100 M_{\odot}/yr$. Such BCGs are found in “cool-core” (“CC”) clusters, and their star formation is thought to be fueled by “cooling flow.” To further investigate the implications of low-redshift, star-forming BCGs, we perform a systematic search using the $22\mu\text{m}$ data (“W4” band) from the Wide-field Infrared Survey Explorer (WISE) on the GMBCG catalog, which contains 55,424 BCGs at $0.1 \lesssim z \lesssim 0.55$ identified in the Sloan Digital Sky Survey (SDSS). Our sample consists of 389 BCGs that are bright in W4 (“W4BCGs”), most being brighter than 5 mJy. While some ($\lesssim 20\%$) might host AGN, most W4BCGs should owe their strong mid-IR emissions to dust-enshrouded star formation. Their median total IR luminosity (L_{IR}) is $5 \times 10^{11} L_{\odot}$ (SFR $\sim 50 M_{\odot}/yr$), and 27% of the whole sample has $L_{IR} > 10^{12} L_{\odot}$ (SFR $> 100 M_{\odot}/yr$). Using ten W4BCGs that have *Chandra* X-ray data, we show that seven of them are possibly in CC clusters. However, in most cases (five out of seven) the mass deposition rate cannot account for the observed SFR. This casts doubt to the idea that cooling flows are the cause of the star formation in non-quiescent BCGs.

Keywords: galaxy clusters, brightest cluster galaxy, galaxy evolution

1. INTRODUCTION

A Brightest Cluster Galaxy (BCG), as the name implies, resides within a galaxy cluster and is its brightest member. BCGs are among the most luminous and the most massive galaxies in the low-redshift universe, usually have little ongoing star formation, and are dominated by old stellar populations (e.g., Dubinski 1998). It is believed that they have assembled most of their stellar masses before $z \sim 3$ (e.g., De Lucia et al. 2006), and have been passively evolving ever since. For this reason, they are among the so-called “red-and-dead” galaxy population.

BCGs being largely quiescent in the low-redshift universe is consistent with the general picture of “downsizing” galaxy evolution (Cowie et al. 1996), where the bulk of the star formation activities in the universe shift from high mass galaxies to low mass ones as the universe evolves. On the other hand, it has been known for over a decade that some BCGs at low redshifts still exhibit significant star formation. Such BCGs are in “cool-core” clusters, whose intra-cluster medium (ICM) has a temperature gradient such that materials can be funneled to the central region where the BCGs reside and presumably can fuel the observed star formation (e.g., O’Dea et al. 2005; Vikhlinin et al. 2007; Santos et al. 2008; Fogarty et al. 2015; see also Donahue et al. 2015 for recent discussions). However, it is unclear what fraction of BCGs still have ongoing star formation.

In this paper, we present a systematic study of star-forming BCGs, using the data from the Sloan Digital Sky Survey (SDSS; York et al. 2000) and the Wide-field In-

frared Survey Explorer (WISE; Wright et al. 2010). We make use of the GMBCG catalog of Hao et al. (2010), which is the largest BCG catalog available to date, and select those BCGs that potentially have strong ongoing star formation activities based on their properties in the mid-IR bands of WISE. Our goal is to shed new light to the understanding of star-forming BCGs as a whole: how rare they are, how high their star formation rates (SFRs) can be, whether they have different properties in other aspects as compared to the vast majority of BCGs that are quiescent, and whether residing in “cool-core” clusters is a satisfactory explanation to their SFRs.

This paper is organized as follows. In Section 2, we briefly describe the data that we use to select star-forming BCGs. The details of the selection process is given in Section 3, and these are followed by Section 4 where we show various diagnostics to separate AGN activity from star formation. In Section 5, we analyze a small subsample of star-forming BCGs that have archival X-ray data that allow us to address various questions regarding their connection to cool-core clusters. We present a discussion of our findings in Section 6, and a summary in Section 7.

Throughout this paper, we adopt the concordant Λ CDM cosmological model of $H_0 = 70 \text{ Mpc}^{-1} \text{ km s}^{-1}$, $\Omega_M = 0.27$, and $\Omega_{\Lambda} = 0.73$. All magnitudes are in AB system unless otherwise noted.

2. DATA

The critical data sets used to select star-forming BCGs are the SDSS-based GMBCG catalog and the WISE all-sky survey data. In particular, we adopt the “un-blurred” version of the WISE data (also known as “un-WISE”) of Lang (2014) for this study. A small number of such selected BCGs also have far-IR (FIR) data from

[†] email: jmr24f@mail.missouri.edu

[‡] email: yanha@missouri.edu

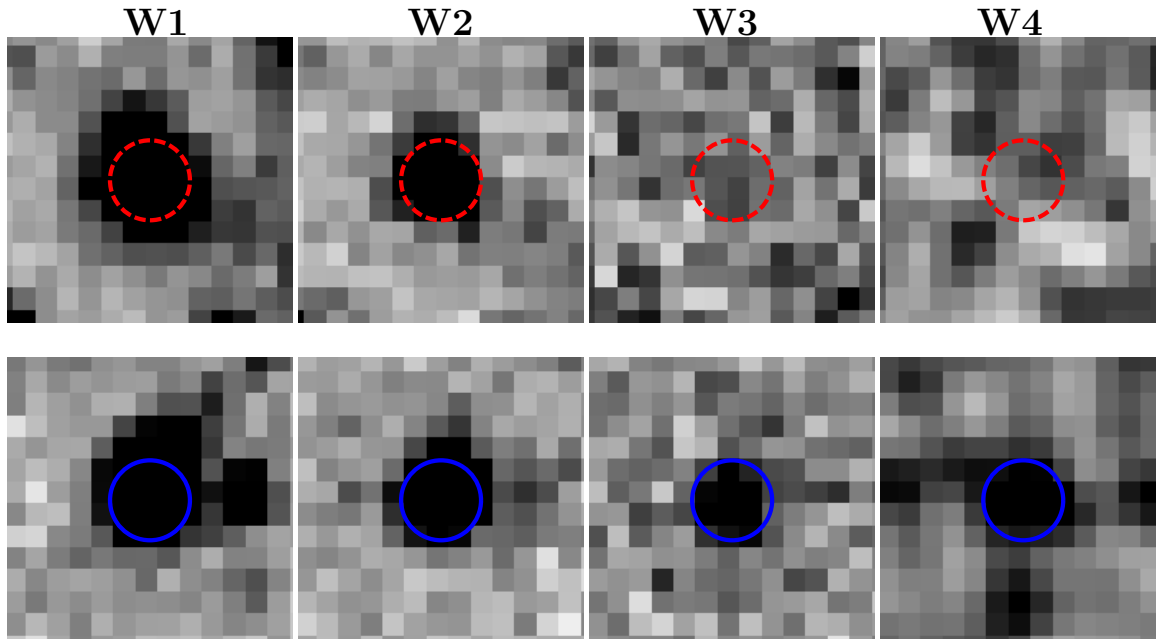


Figure 1. Examples showing WISE 4-band images of a BCG that is undetected in the W4 band (top) and one that is detected (bottom). These image cutouts are made from the unWISE products. The circles are centered on the reported SDSS positions, and are $10''$ in radius.

Herschel or X-ray data from *Chandra*, which we used for further analysis. All these data are briefly described below.

2.1. GMBCG Catalog

The GMBCG Catalog (Hao et al. 2010) consists of 55,424 rich galaxy clusters found by using the Gaussian Mixture Brightest Cluster Galaxy (GMBCG) algorithm on the SDSS data in the seventh data release (DR7). This algorithm detects clusters by identifying the BCG and the red sequence galaxies in its vicinity and calculating the clustering strength, a measure of the surface density of cluster galaxies at the BCG position. Hao et al. (2010) apply this method to the Legacy Survey Area of SDSS DR7, which covers $7,300 \text{ deg}^2$ of the North Galactic Cap and 740 deg^2 from three stripes in the South Galactic Cap, and obtain their cluster catalog across the redshift range $0.1 \lesssim z \lesssim 0.55$.

This GMBCG catalog contains the positions of the identified BCGs along with their redshifts and photometry. The redshifts are either spectroscopic redshifts ($\sim 20,000$ objects) or photometric redshifts (see Hao et al. 2010 for details).

2.2. WISE and unWISE

The nominal WISE mission mapped the entire sky in 2010 in four near-to-mid-IR bands, namely, W1, W2, W3, and W4, whose central wavelengths are 3.4, 4.6, 12, and $22 \mu\text{m}$, respectively. The spatial resolutions in these four bands are $6.1''$, $6.4''$, $6.5''$, and $12.0''$, respectively. The nominal 5σ limits in these bands are 0.068, 0.098, 0.86 and 5.4 mJy , respectively (Wright et al. 2010).

The officially released images of WISE (“AllWISE”) were intentionally convolved by the point spread functions (PSFs) during the co-adding process. While this process is appropriate for isolated point sources, it reduces the resolution of the images and thus exacerbates the blending problem. To remedy this problem, un-

WISE¹ (Lang 2014) “un-blurs” these images to produce the final stacks that preserve the native spatial resolutions.

Along with the un-blurred images, unWISE also provides a catalog of WISE photometry based on “forced photometry” using ~ 400 million SDSS DR10 objects as the morphological templates to fit the WISE source light profiles (Lang et al. 2014). Since the GMBCG catalog is based upon the same SDSS data (albeit in an earlier data release), all of our objects appear in the unWISE forced photometry catalog. Therefore, we adopted the unWISE images for visual verification and its forced photometry for quantitative analysis.

2.3. *Herschel* data

In order to further study the star formation properties of the selected BCGs, we also used the archival FIR data taken by the Spectral and Photometric Imaging Receiver (SPIRE; Griffin et al. 2010) on *Herschel* Space Observatory (Pilbratt et al. 2010). While only a small number of objects have these SPIRE data, they offer a valuable reference that we will detail in §4.3.

Specifically, we made use of the SPIRE three-band (250 , 350 and $500 \mu\text{m}$) photometry from the following *Herschel* very wide-field surveys whose SPIRE data are now publicly available, namely, the *Herschel* Multi-tiered Extragalactic Survey (HerMES; Oliver et al. 2012; Roseboom et al. 2010; Smith et al. 2012; Viero et al. 2013; Wang et al. 2014), the *Herschel* Stripe 82 Survey (HerS; Viero et al. 2014) and the *Herschel* Astrophysical Terahertz Large Area Survey (H-ATLAS; Eales et al. 2010; Valiante et al. 2016). Both HerMES and H-ATLAS have catalogs available that include flux measurements. For the HerS data, we measured the source flux on the SPIRE images using HIPE (Ott 2010) following the procedure for source extraction and photometry outlined in

¹ <http://unwise.me>

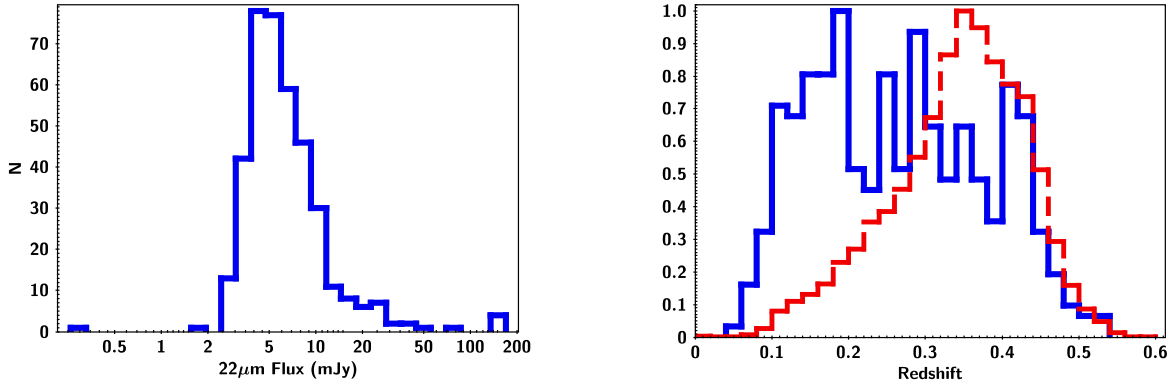


Figure 2. Left: W4 ($22\ \mu\text{m}$) flux density distribution of the W4-detected BCGs (W4BCGs). Right: Normalized redshift distribution for the entire GMBCG catalog (red dashed line) and the subset of W4BCGs (blue solid line).

the SPIRE data manual². In total, these surveys cover $340\ \text{deg}^2$.

2.4. Chandra Data

In order to investigate possible cool-core properties of our sample, X-ray data is necessary. Therefore, we used the public *Chandra* X-ray data provided by the Chandra Data Archive. Both Primary and Secondary products were retrieved for each available observation. These data provide a spatial resolution of $0.5''$ and cover an energy range of 0.1-10 keV.

Standard data processing was carried out starting from the level 1 event files using CIAO 4.8.2 (Fruscione et al. 2006) with CALDB 4.7.0 of the *Chandra* Calibration Database. The reprocessing script *chandra_repro* was used to reprocess the data and create level 2 event files. When observations were taken in the VFAINT mode, the parameter *check_vf_pha* was set to “yes” in order to remove background events likely caused by cosmic rays. Background estimates were taken in the same field away from the central X-ray peak and clear of any other X-ray sources.

For X-ray spectra, we followed a procedure similar to that of Molendi et al. 2016 (hereafter Mol16). The X-ray spectra for the BCG were processed from the level 2 event files using *specextract* in CIAO. A 40 kpc region centered on the BCG was chosen for the extraction. There could be a complication in this analysis if the BCG is an X-ray AGN, in which case the X-ray spectrum might be dominated by the AGN rather than the heated ICM. To solve this potential problem, we performed a separate analysis by following Mol16 and masking the central region. Unlike in Mol16 where a circular region of $2''$ in radius is masked, we chose to only mask out the inner 2 kpc of the BCG, as choosing a global value of $2''$ would result in masking out the bulk of X-ray flux for some of our sources. Background spectra were also processed at up to three different regions away from the X-ray peak and any other X-ray sources.

3. SAMPLE OF BCGS WITH STRONG MID-IR EMISSION

We searched for BCGs with ongoing star formation by identifying those that have secure mid-IR detections in

the WISE W4-band at $22\ \mu\text{m}$. This will reveal dust-embedded star formation in BCGs, and thus is complementary to the method that aims at identifying unobscured star formation through UV emissions, such as some of those reported by Donahue et al. (2015). Here we describe our sample in detail.

3.1. Initial Selection

To construct a catalog of possible sources that have W4 detection, the GMBCG catalog was cross-matched with the unWISE forced photometry catalog using a matching radius of $5''$, which is slightly less than half the spatial resolution of W4. We further required that a matched object should have $S/N \geq 5$ in W4 as reported in the unWISE SDSS forced photometry catalog. This resulted in 1,323 BCGs in our initial sample.

To ensure the sample robustness, we visually inspected the images of all these initial candidates. We found that a large number of the reported W4-detections were actually false-positives due to various reasons, such as image defects, noise spikes, artifacts produced by a bright neighbor, etc. After rejecting these contaminants, 458 BCGs survived. As an example, Fig. 1 shows the WISE image stamps of one that is not detected in W4 and one with a real W4-detection.

3.2. Sample Verification

Obviously, W4-detected BCGs are only a small fraction of the entire GMBCG sample. Therefore, we must consider possible contamination to the GMBCG sample, or in other words, whether these W4-detected objects derived from the GMBCG sample are BCGs at all. To address this question, we further verified the legitimacy of these 458 candidate objects on a one-by-one basis. This verification was to decide whether a candidate is in a cluster environment, and if yes, whether it is the BCG of the cluster. Our intention was not to invent a new cluster finding algorithm, but to perform an independent “sanity check” on the claimed BCGs.

The verification consisted of two steps. First, we worked under the assumption that the photometric redshifts that the GMBCG catalog relies on are accurate enough for its purpose. We used the SDSS DR7 data, the same as what the GMBCG catalog is based. For each candidate BCG, we retrieved the objects within a

² <http://herschel.esac.esa.int/hcss-doc-12.0/>

3' radius around it, and retained only those whose photometric redshifts (as reported in the SDSS DR7) were within ± 0.02 of the redshift of the candidate BCG (as quoted in the GMBCG catalog and is the same as in the SDSS DR7). The retained objects were considered as the members of the candidate cluster. This redshift range was adopted because it is the reported accuracy (1σ) of the SDSS DR7 photometric redshifts. We then constructed the i vs. $(g-r)$ color-magnitude diagram, and checked whether we could see a “ridge line” indicative of a red sequence. If a red sequence was seen, we checked whether the current candidate BCG was the correct identification of BCG, i.e., whether it was the brightest one (in i -band) among all members.

After this step, we confirmed that 383 objects survived. Among the 75 dubious cases, four could hardly be called clusters because they only had a few members (< 8), and thus must be rejected. These four sources were at the high-redshift end of the catalog. One other case was a misidentification, and actually must be part of Abell 1689 (whose BCG is already in the W4BCG sample) and thus must also be removed. The other 70 objects were in clusters with a clear red sequence, however they were in fact not the BCGs. Therefore, we identified the “new” BCG for each of these 70 cases by finding the brightest member, and conducted all the previous steps reported above on these “new” BCGs. Of all these 70 objects, only six have reliable W4 detections. We included these six objects into our sample, and thus our final sample consists of 389 objects in total.

3.3. General Properties and Subdivision of the Final Sample

Fig. 2 shows the distributions of their W4 flux densities and redshifts. At these redshifts, the W4 emissions are still in the rest-frame mid-IR, and must be originated from heated dust instead of stellar continuum. These W4-detected BCGs (hereafter “W4BCGs”) comprise a special population at odd with the general picture of BCGs that they are old, passively evolving galaxies. Therefore, we aim to understand the nature of these exceptions.

In order to investigate whether the occurrence of W4BCG could be dependent of the cluster richness, we divide our final W4BCG sample into two categories based on the reported GMBCG cluster richness (“ N_{gals}^{scaled} ”) in Hao et al. (2010). We adopt $N_{gals}^{scaled} = 15$ as the criterion, and refer to those clusters with $N_{gals}^{scaled} \geq 15$ as “rich” clusters and those with $N_{gals}^{scaled} < 15$ as “poor” clusters. The rich clusters are 28% of the entire GMBCG sample, while the poor clusters make of 72%. The corresponding W4BCGs are subsequently divided into the W4BCG-R (108 objects, or 27.8% of the total 389 W4BCGs) and the W4BCG-P (281 objects, or 72.2%) subsamples, respectively.

4. DATA ANALYSIS

There are two possible causes to the heated dust emissions of these W4BCGs in the mid-IR, namely, active ongoing star formation or AGN activities. In this section, we investigate which of these two mechanisms is the more probable cause.

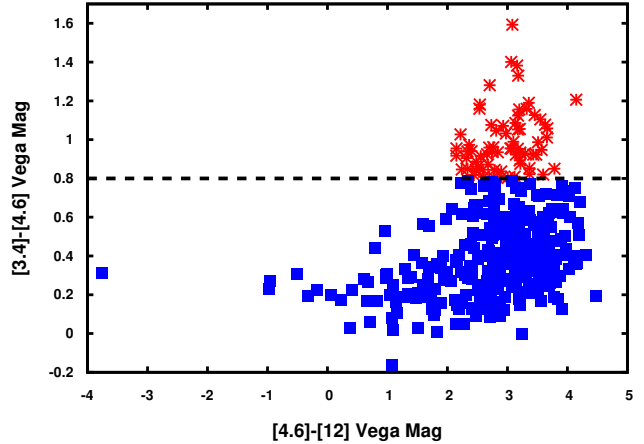


Figure 3. WISE color diagnostics of W4BCGs. The dashed line at $W1 - W2 = 0.8$ mag (Stern et al. 2012) separates AGN (red asterisks) and non-AGN (blue squares). Only 69 out of the total 389 W4BCGs are possible AGN hosts by this selection.

4.1. Possible AGN Hosts

To understand whether any of our W4BCGs could possibly host an AGN, we performed two diagnostics, which are based on the WISE color selection and the BPT diagram method, respectively. We note that being diagnosed as an AGN host by either method does not necessarily mean that the mid-IR emission in W4 must be dominated by AGN heating. However, if we do not find any AGN activity by either method, it is very plausible that the mid-IR emission is mainly driven by the heating of star formation.

4.1.1. WISE Color Diagnostics

Using a $W1 - W2$ versus $W2 - W3$ WISE color-color plot has been shown to be an effective method to identify AGN (Jarrett et al. 2011; Mateos et al. 2012; Stern et al. 2012; Assef et al. 2013). Furthermore, it has been demonstrated that a single color criterion of $W1 - W2 \geq 0.8$ mag (in Vega system) provides a robust selection of AGN (Stern et al. 2012; Assef et al. 2013). We adopted this latter method in our analysis, and the result is shown in Fig 3. We find that only 69 out of the total 389 W4BCGs and 12 of the 108 W4BCG-Rs satisfy this criterion (17.7% and 11.1% respectively), or in other words, most W4BCGs should be dominated by starbursts.

4.1.2. BPT Diagram

BPT diagrams are a set of diagnostic diagrams using emission lines to determine the ionization mechanism of nebular gas. The most commonly used diagram is $[\text{OIII}]5007/\text{H}\beta$ versus $[\text{NII}]6584/\text{H}\alpha$ (Baldwin, Phillips, & Terlevich 1981), which is what we used in our analysis. Various dividing curves have been proposed to separate AGN from star-forming galaxies (e.g. Kewley et al. 2001; Kauffmann et al. 2003a). The curve of Kauffmann et al. (2003a), which is shown in Eq. 1 below, is the most aggressive in selecting AGN, and hence we adopted this selection criterion in order to be conservative in attributing W4BCGs to starburst:

$$\log([\text{OIII}]/\text{H}\beta) = 0.61 / (\log([\text{NII}]/\text{H}\alpha) - 0.05) + 1.3. \quad (1)$$

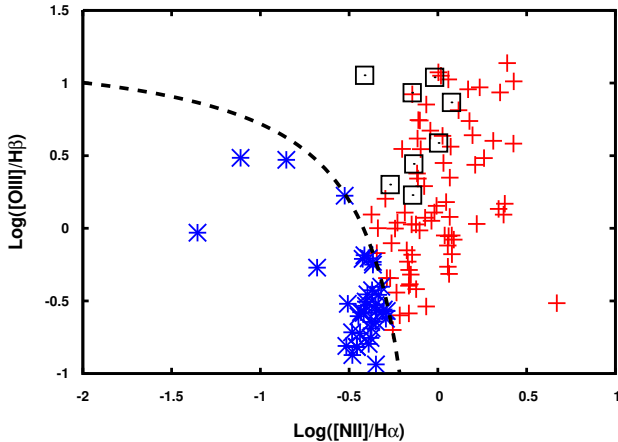


Figure 4. BPT diagnostics of W4BCGs. The dashed curve represents the criterion of Kauffmann et al. (2003) that separates AGN-dominated objects (red pluses) and star-forming-dominated objects (blue asterisks). The black open squares (8 in total) indicate those that are also deemed to be AGN hosts based on the WISE color selection (see Fig. 3.)

For emission line measurements, we used the MPA-JHU (Max-Planck Institute for Astrophysics - John Hopkins University) “value-added” DR7 catalog of spectrum measurements (Brinchmann 2004; Kauffmann et al. 2003b; Tremonti et al. 2004) based on the SDSS DR7 data. A cross-match to the MPA-JHU catalog (within a radius of 5'' of the GMBCG reported position) resulted in 123 objects with emission line measurements for all four lines needed for the BPT diagnostic, which is shown in Fig 4. Within this subsample of 118 W4BCGs, 84 are deemed to host AGN (29 are W4BCG-R).

4.2. Morphology

The morphologies of the W4BCGs may provide additional information to reveal the nature of their mid-IR emissions. In particular, we are interested in understanding whether merger could be relevant, regardless of the exact heating source being AGN activities or star formation. For this purpose, the SDSS i' band images were examined. The W4BCGs were then divided into three different categories: “Merger”, where a recent or ongoing merger is evident as shown by disturbed morphology; “Close Neighbor”, where there is no clear sign of merger but there is at least one galaxy within 10'' (even though this could be due to projection by chance); and “Single”, where there is no sign of merger and no other galaxies within 10'' to the SDSS depth. Some examples are shown in Fig. 5. We note that 10'' corresponds to 18–60 kpc at the redshifts of the W4BCGs.

The statistics are listed in Table 1, which shows that the majority of W4BCGs do not exhibit obvious merger properties. Therefore, it is safe to conclude that the mid-IR emission of a W4BCG is independent of whether it is interacting with others.

4.3. Star Formation Rates

The analysis above clearly shows that most W4BCGs are not AGN hosts, and hence their mid-IR emission can only come from dust heated by strong star formation. Again, this is contrary to the general picture that BCGs are “red-and-dead” galaxies that have ceased their

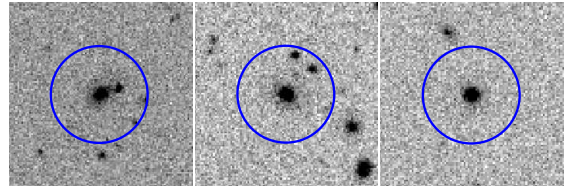


Figure 5. SDSS i' band images illustrating the different morphology subsets. Left: A BCG with obvious merger properties. Middle: A BCG with a neighbor within 10'' but no obvious merger properties. Right: A BCG with no other galaxies within a 10'' radius.

Table 1

Morphology of W4 detected BCGs based on SDSS i' images

Type	Count
Merger	69
Close Neighbor	145
Single	175

star formation long ago. This also leads to the question whether the mid-IR emissions of those AGN-hosting W4BCGs are due to AGN heating at all, as our data currently available cannot provide an unambiguous answer. In this section, we attempt to derive the star formation rates of the W4BCGs as a whole, assuming that the AGN contribution to their mid-IR emissions is negligible. In our later discussion, we examine whether this assumption is reasonable.

4.3.1. SED Fitting

A common method to derive IR-based SFR is to calculate the total IR luminosity (L_{IR}) over the conventional range of 8–1000 μm and then to infer the SFR by using the relation of Kennicutt (1998) as follows:

$$SFR[M_{\odot}/yr] = 1.0 \times 10^{-10} L_{IR}[L_{\odot}]. \quad (2)$$

We note that the coefficient in the above equation is after adjusting to a Chabrier (2003) initial mass function (IMF) and the derived SFR is a factor of 1.7 smaller than in case of using a Salpeter (1955) IMF.

L_{IR} can be calculated by fitting the spectral energy distributions (SEDs) to appropriate templates of dusty star forming galaxies (e.g., Chary & Elbaz 2001; Dale & Helou 2002; Siebenmorgen & Krügel 2007). In our case, W3 and W4 can be used for this purpose. We are also interested in the properties of the stellar populations in the W4BCGs, such as stellar mass and age, which can be derived by fitting the SEDs at the bluer wavelengths to stellar population synthesis models. Therefore, we utilized LePhare (Arnouts et al. 1999; Ilbert et al. 2006), which is capable of fitting both the stellar populations and the heated dust components at the same time.

Our input SEDs were constructed using the SDSS DR7 photometry in conjunction with the unWISE photometry (as described in §2.2) to cover the optical to mid-IR regime. The heated dust emission was fit to the template of Siebenmorgen & Krügel (2007; SK07), and the fit was confined to the W3 and W4 bands only. For the stellar component, the fit included the five SDSS bands as well as the W1 and W2 bands. LePhare treats the transition of stellar emission and heated dust emission in a consistent manner; i.e., the contribution of the dust emission template to the bands bluer than W3 (or that

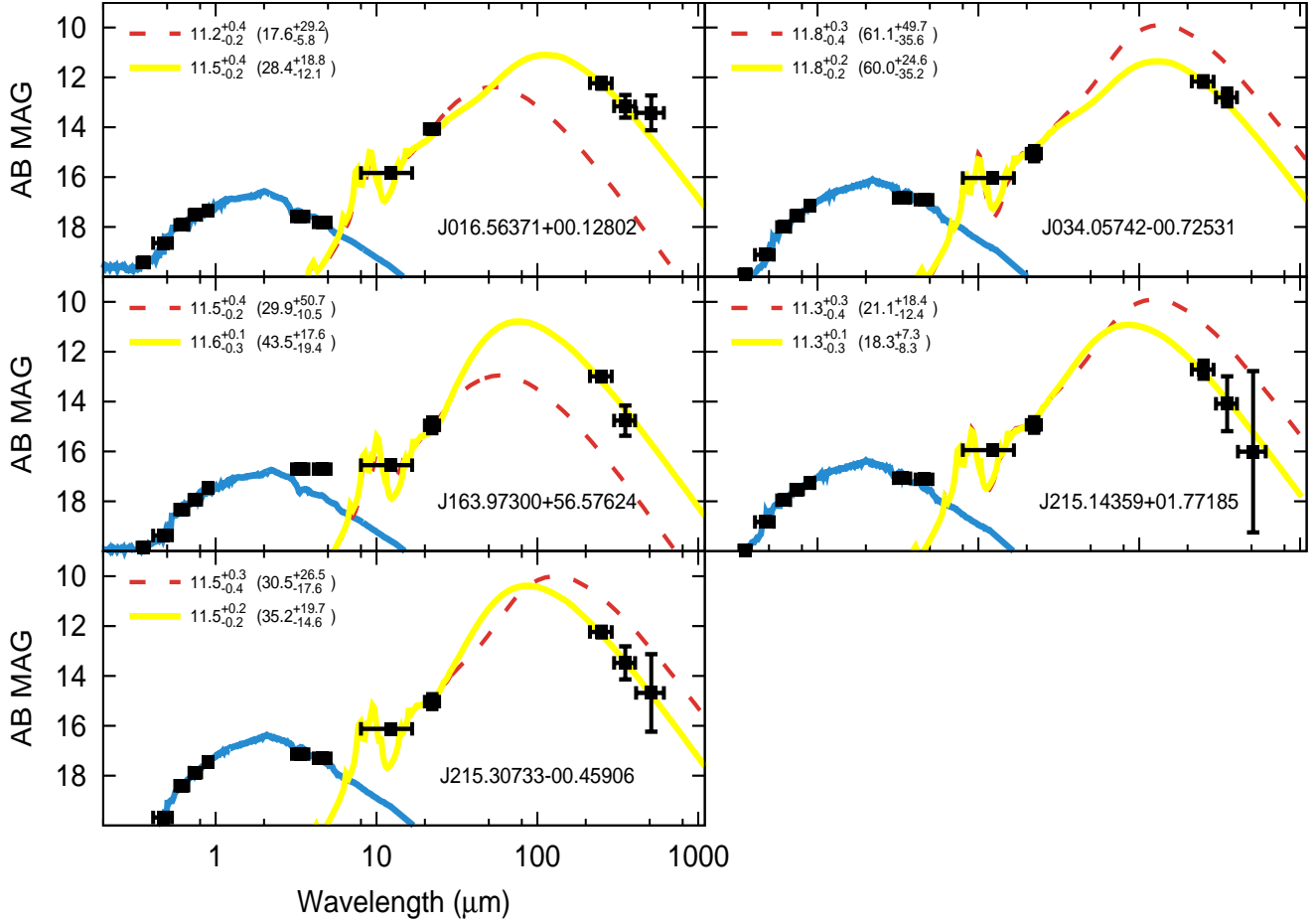


Figure 6. Spectral energy distributions of the subsample of five W4BCGs that have *Herschel* data. The fitting of their stellar populations (shown by the blue curve) is the same as in the other W4BCGs, which incorporates both the SDSS photometry in optical and W1 and W2 in near-IR (see text for details). Two fitting schemes in the mid-to-far-IR regime are shown: one only using WISE data (dashed red) and one including *Herschel* data (solid yellow). The blue curve shows the SED fitting results of the stellar populations, which incorporate the SDSS photometry in optical and the WISE near-IR photometry in W1 and W2. The $\log(L_{IR})$ value is displayed in the top left for each fitting along with the corresponding SFR (in M_{\odot}/yr) in parenthesis.

Table 2
Summary of the Subset with *Herschel* Data

GMBCG Catalog Name	250 μm (mJy)	350 μm (mJy)	500 μm (mJy)	$\text{Log}(L_{IR}/L_{\odot})$ No SPIRE	$SFR_{NoSPIRE}$ (M_{\odot}/yr)	$\text{Log}(L_{IR}/L_{\odot})$ w/ SPIRE	SFR_{SPIRE} (M_{\odot}/yr)
W4BCG-R							
J034.05742-00.72531	49.57 \pm 5.92	27.54 \pm 5.40	–	11.79 $^{+0.26}_{-0.38}$	61.12 $^{+49.67}_{-35.60}$	11.78 $^{+0.20}_{-0.23}$	59.99 $^{+35.22}_{-24.56}$
W4BCG-P							
J016.56371+00.12802	46.39 \pm 5.84	19.81 \pm 4.81	15.50 \pm 5.42	11.25 $^{+0.43}_{-0.17}$	17.61 $^{+29.24}_{-5.82}$	11.45 $^{+0.22}_{-0.24}$	28.41 $^{+18.83}_{-12.15}$
J163.97300+56.57624	23.21 \pm 1.92	4.52 \pm 1.41	–	11.48 $^{+0.43}_{-0.19}$	29.88 $^{+50.69}_{-10.52}$	11.64 $^{+0.15}_{-0.26}$	43.51 $^{+17.55}_{-19.43}$
J215.14359+01.77185	29.79 \pm 5.93	8.43 \pm 4.15	1.43 \pm 1.23	11.32 $^{+0.27}_{-0.39}$	21.13 $^{+18.37}_{-12.44}$	11.26 $^{+0.15}_{-0.26}$	18.30 $^{+7.27}_{-8.32}$
J215.30733-00.45906	46.00 \pm 5.64	14.76 \pm 4.95	4.87 \pm 3.00	11.48 $^{+0.27}_{-0.37}$	30.52 $^{+26.51}_{-17.59}$	11.55 $^{+0.19}_{-0.23}$	35.19 $^{+19.68}_{-14.56}$

Note: *Herschel* SPIRE photometry are either adopted from the public data releases from the relevant teams when available (DR2 of HerMES and DR1 of H-ATLAS) or based on our own source extraction (for those objects in HerS) using HIPE (Ott 2010).

of the stellar emission template to the bands redder than W2), albeit small, is still considered during the simultaneous fit of the two components. The stellar component was fit to the stellar population synthesis models of Bruzual & Charlot (2003; hereafter BC03). We adopted the BC03 models of solar metallicity and the Chabrier IMF, and used a series of exponentially declining star formation histories with τ ranging from 1 Myr to 20 Gyr. We note that we chose solar metallicity because we do

not have any constraint on the metallicities of these objects, and the solar metallicity is the most widely adopted value throughout the literature in such case. The models were allowed to be reddened by dust following the Calzetti’s law (Calzetti 2001), with the reddening color excess value, $E(B-V)$, allowed to vary over three ranges: from 0 up to 0.5 mag, from 0 up to 0.3 mag, and fix to zero (i.e., no reddening). While the W4BCGs have very dusty star-forming regions, their exposed stellar popu-

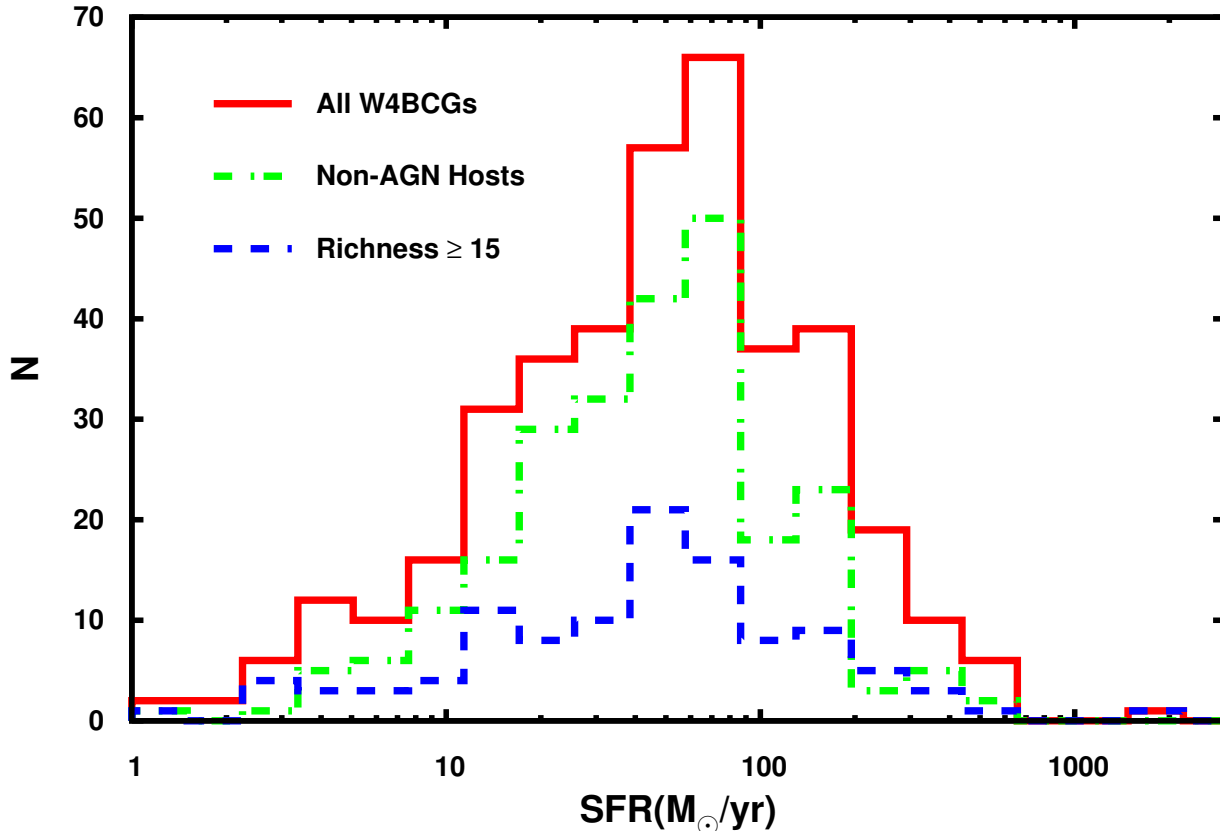


Figure 7. A histogram of the derived SFR for the entire W4BCGs sample (red solid line), the non-AGN host subset (green dot-dashed), and the subset with richness ≥ 15 (blue dashed line; regardless of hosting AGN or not).

lations as seen in optical-to-near-IR are not necessarily dusty. As the reddening parameter and the age of the stellar population are degenerated, we tested these three different choices to investigate the impact of different reddening values to the derived ages. Redshifts were fixed to those provided by the GMBCG Catalog.

4.3.2. Far-IR Constraint from Herschel

As W3 and W4 only sample a small mid-IR window of the entire rest-frame 8-1000 μm range, it could be a concern whether they can accurately “anchor” the fitting templates to derive L_{IR} . A large number of practices in the literature have shown that one or two mid-IR bands indeed can derive L_{IR} reasonably well (see e.g. Chary & Elbaz 2001; Magnelli et al. 2009; Elbaz et al. 2010; Dale et al. 2014), except that in the very high luminosity range such results tend to overestimate the true L_{IR} (see e.g., Elbaz et al. 2011 and the references therein). In order to check how well our derivation of L_{IR} above can be, we tested a few objects that also have FIR SPIRE data as described in §2.4, which samples the peak of the dust emissions and thus offers the most reliable derivation of L_{IR} to date.

Following the same procedure of Ma & Yan (2015), we found secure SPIRE counterparts within a matching radius of $3''$ for five W4BCGs: 2 in HerS, 1 in HerMES, and 2 in H-ATLAS. A summary of the data is given in Table 2. We ran LePhare to fit the SEDs of these objects as before, but with the SPIRE photometry added. Fig. 6 shows their SED fitting results. For these five objects, we

find that the derived median L_{IR} values with and without the inclusion of the SPIRE data differ by ~ 0.1 dex on average and 0.3 dex at most. Therefore, we believe that using W3 and W4 photometry to derive total L_{IR} based on starburst templates (as in §4.3.1) is applicable.

4.3.3. Results

Applying Eq. 2 to our sample of 389 W4BCGs results in SFRs ranging from a few to $\sim 1000 M_{\odot}/\text{yr}$ (Fig. 7). The median L_{IR} is $5 \times 10^{11} L_{\odot}$ (or SFR $\sim 50 M_{\odot}/\text{yr}$), and 27% of the whole sample has $L_{IR} > 10^{12} L_{\odot}$ (or SFR $> 100 M_{\odot}/\text{yr}$). The statistics largely remain the same even if we only look at W4BCG-Rs or W4BCG-Ps, or if we remove any possible AGN hosts from the sample. Obviously, the W4BCGs are not “dead”, i.e., they are not simply passively evolving like the BCG majority at low redshifts.

In addition to L_{IR} , SED fitting also derives stellar mass and age for each object. To check whether these W4BCGs have different stellar population properties as compared to the BCG majority, we performed SED fitting for all the non-W4BCGs from the entire GMBCG set in the same way as described in §4.3.1. The SEDs were based on the SDSS photometry and the unWISE photometry in W1 and W2. Fig. 8 compares the stellar mass and the age distributions of the W4BCGs to those of the non-W4BCGs. As expected from the reddening-age degeneracy, the ages of the W4BCGs show somewhat different trends with respect to the non-W4BCGs under different choices of allowed reddening range. This

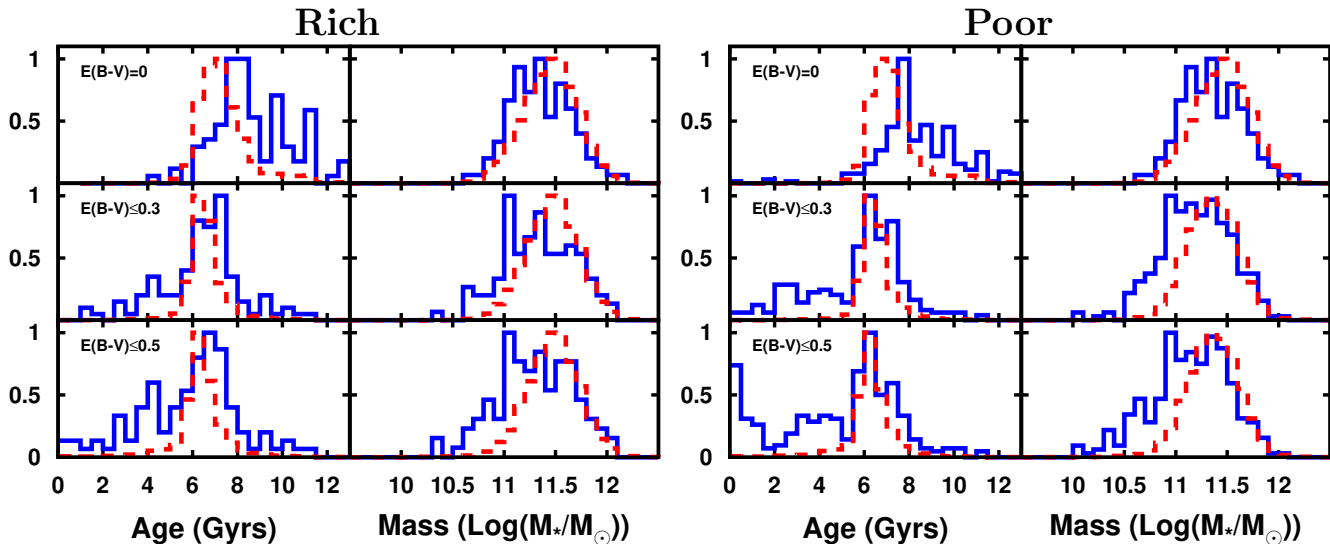


Figure 8. Left: Histogram distribution of the derived ages and masses for the “Rich” subset (richness ≥ 15) among W4BCGs (solid blue) and the GMBCG catalog (dashed red) for $E(B-V)$ max values of: 0 (top), 0.3 (middle), and 0.5 (bottom). Right: Same as left except with the “Poor” subset (richness < 15).

is further complicated by the fact that our SED fitting templates are fixed to solar metallicity. There is also an age-metallicity degeneracy in SED fitting, in the sense that adopting a lower metallicity could result in an older age. Therefore, no definite difference in trend can be claimed regarding the age comparison. The differences in stellar mass, on the other hand, show less variation in the trends under the three choices of allowed reddening ranges. Overall speaking, we believe that the W4BCGs do not show obvious differences as compared to the non-W4BCGs in mass and age of their exposed stellar populations.

5. COOL-CORE CLUSTERS

As mentioned in §1, it has been reported in the literature that some BCGs do exhibit ongoing star formation. While their SFR triggering mechanism is unclear, they are believed to reside in “cool-core” clusters (e.g. Molendi & Pizzolato 2001; O’Dea et al. 2005; Vikhlinin et al. 2007; Chen et al. 2007; Santos et al. 2008; Hudson et al. 2010; Donahue et al. 2015; McDonald et al. 2016; Molendi et al. 2016). Most of these previously reported star-forming BCGs in cool-core clusters have much lower SFR as compared to the bulk of our W4BCGs, with the most notable exception of the BCG in the Phoenix cluster at $z = 0.597$ (McDonald et al. 2012; Tozzi et al. 2015; Mittal et al. 2017), which has $SFR \sim 450 M_{\odot}/yr$ (after scaling to the Chabrier IMF). In this section, we consider whether our W4BCGs reside in cool-core clusters (hereafter “CC clusters”) as well, which can be determined by analyzing X-ray data.

5.1. Archival Chandra Data

We searched the *Chandra* archive and found that 10 W4BCGs have existing data. All observations were obtained using the ACIS instrument in either FAINT or VFAINT mode. Table 3 summarizes these data.

5.2. X-ray c_{SB} Parameter

Typically, a central X-ray surface brightness excess is a good indicator of a cool core (Fabian & Nulsen 1977). Following this idea, Santos et al. (2008) investigate the surface brightness concentration of galaxy clusters in the central region, and propose a parameter, c_{SB} , to distinguish between CC and non-CC clusters.

This parameter is defined as the ratio of the soft X-ray flux within 40 kpc and within 400 kpc (Santos et al. 2008):

$$c_{SB} = \frac{F_{r < 40kpc}}{F_{r < 400kpc}} \quad (3)$$

These radii are chosen because they result in the largest difference between CC and non-CC clusters. The value for c_{SB} can be divided into three different regimes (Vikhlinin et al. 2007; Santos et al. 2008): non-CC ($c_{SB} < 0.075$), moderate CC ($0.075 < c_{SB} < 0.155$), and strong CC ($c_{SB} > 0.155$). Following Santos et al. (2010), we adopted the 0.5-2.0 keV band for the soft X-ray flux measurement.

Fig. 9 shows the values of c_{SB} for all the sources with *Chandra* observations. As is quite apparent, the value for c_{SB} puts seven out of ten of these objects in the strong CC region, although two might have contamination due to AGN activity. However, there are three clusters not detected in X-ray at all, which we will discuss later in §5.4.

5.3. X-ray Spectral Fitting

For these seven CC clusters we further investigate their properties by carrying out X-ray spectral fitting. The spectra were fit using XSPEC 12.9.0 (Arnaud 1996) and a cooling flow model `mkcflow` (Mushotzky & Szymkowiak 1988) coupled with a single-temperature `mekal` model (Mewe et al. 1985, 1986; Kaastra 1992; Liedahl et al. 1995). We follow the same procedure outlined in §3.2 of Mol16 for the first method to find the spectral mass deposition rate. The minimum temperature for the `mkcflow` model was frozen to 0.15 keV, while the maximum temperature was frozen to 3.0 keV. The minimum tempera-

Table 3
Summary of Available Archival *Chandra* Data

GMBCG Catalog Name	ObsID	<i>Chandra</i> Target Name	RA(J2000) ^a	DEC(J2000) ^a	z^b	Exptime (ks)	$F_{r<40kpc}$ ($erg/s/cm^2$)	$F_{r<400kpc}$ ($erg/s/cm^2$)
W4BCG-R								
J027.58864-10.09181	11711	MACS J0150.3-1005	1:50:21.27	-10:05:30.50	0.365	26.8	2.27E-13	8.60E-13
J125.25942+07.86314 ^c	1647	RXJ0821	8:21:02.26	7:51:47.30	0.14*	9.4	4.21E-13	2.12E-12
–	17194	RXJ0821.0+0752	8:21:02.26	7:51:47.30	0.14*	29.2	4.04E-13	1.79E-12
–	17563	RXJ0821.0+0752	8:21:02.26	7:51:47.30	0.14*	37.3	4.26E-13	1.78E-12
J128.72875+55.57253 ^c	1645	4C55.16	8:34:54.90	55:34:21.10	0.241	9.1	5.18E-13	1.98E-12
–	4940	4C55.16	8:34:54.90	55:34:21.10	0.241	96.0	7.41E-13	2.14E-12
J160.18541+39.95313	1652	ABELL 1068	10:40:44.50	39:57:11.30	0.138	26.8	1.61E-12	5.54E-12
J219.69392+06.50142	15376	J219.69392+06.50142	14:38:46.54	6:30:05.10	0.403	9.6	<1.81E-15	<6.92E-14
J355.91977+00.34170	5786	ZwCl 2341.1+0000	23:43:40.74	0:20:30.10	0.261	29.8	<3.72E-15	<2.60E-13
W4BCG-P								
J125.63314+05.95189	12730	3C198	8:22:31.95	5:57:06.80	0.082	8.0	<6.38E-15	<3.56E-13
J132.60301+37.78597	11576	6C0850+3747	8:50:24.72	37:47:09.50	0.33*	39.3	1.61E-13	2.43E-13
J133.71068+62.31389	16138	RXJ085451.0+621843	8:54:50.56	62:18:50.00	0.29*	17.7	4.80E-13	5.79E-13
J140.28593+45.64928	827	3C219	9:21:08.62	45:38:57.40	0.174	18.8	5.23E-13	7.78E-13

^a As quoted from the GMBCG catalog

^b Redshifts marked with an asterisk are photometric redshifts

^c J125.25942+07.86314 was observed three times, and J128.72875+55.57253 was observed twice. These data were treated separately in our follow-up analysis.

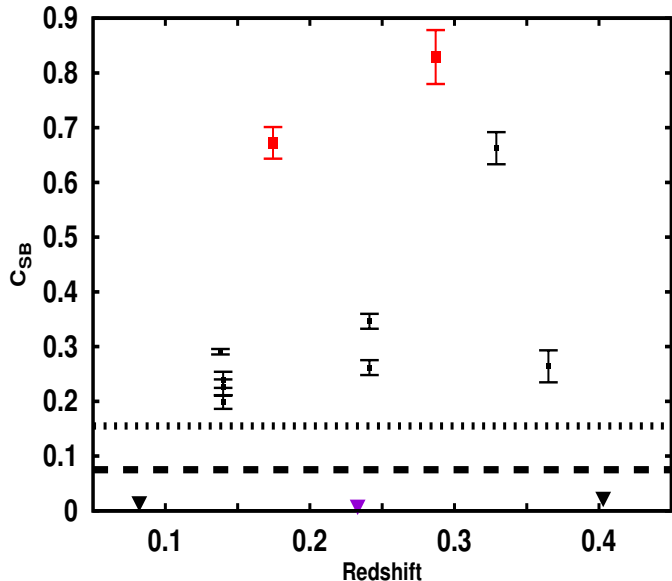


Figure 9. A plot of c_{SB} versus redshift of the 10 W4BCGs that have archival *Chandra* X-ray data. The dashed line at 0.075 separates non-cool-cores from moderate cool-cores. The dot-dashed line at 0.155 separates moderate cool-cores from strong cool-cores. Possible AGN hosts are color coded according to identification method: BPT in blue, WISE color in red, and both in purple. The three data points at $z=0.14$ and the two at $z=0.24$ are for c_{SB} derived using different observations of the same object. The triangle shows the upper limit of the object that has no X-ray detection.

ture for the *mekal* model was set to 4.0 keV. The Galactic absorption was frozen to the value based on the radio map of Kalberla et al. (2005) at the position of the BCG. The *mkcflow* fitting outputs the mass deposition rate (\dot{M}_{dep}) in M_{\odot}/yr .

The fitting results are given in Table 4. Values with no error given represent fits that did not converge (i.e., error was larger than calculated value), and we quote the upper limit based upon the 95% confidence level. Five out of these seven have mass deposition rates falling short of the SFR estimate from L_{IR} . Even for the ones with $\dot{M}_{dep} >$

SFR , it would require a very high efficiency ($\eta > 37\text{--}86\%$) to convert mass into stars so that the observed SFR can be sustained by the cooling flow. Thus, it is unclear whether a possible cooling flow in these CC clusters can be responsible for the observed W4BCG star formation.

This result is in agreement with the recent observations of some BCGs in Moll16, where the mass deposition rate was found to be an order of magnitude lower than the estimated star formation rate. Moll16 provides some possible explanations for this phenomenon, which include an origin of the gas other than the ICM, a delay between cooling and star formation, and, most likely, gas cooling out of the X-ray phase in regions much larger than those measured. However, further investigation is beyond the scope of this paper.

5.4. Lack of Cool-Core?

As shown in the previous section, seven of these W4BCGs are consistent with current theory by residing in cool-core clusters. However, three W4BCG do not have X-ray detection and thus show no sign of being in a cool-core, which could contradict the currently accepted picture. For these objects, the upper limit of the soft X-ray flux within a 40 kpc aperture is no larger than $2 \times 10^{-15} \text{ erg s}^{-1} \text{ cm}^{-2}$ (for comparison, the detected sources have fluxes on the order of $10^{-13}\text{--}10^{-12} \text{ erg s}^{-1} \text{ cm}^{-2}$). Here we discuss them briefly:

J219.69392+06.50142

This W4BCG is at $z_{spec}=0.4029$, which is the most distant one in the X-ray sample. However, its exposure time of only 9.6 ks puts it at the shallow end of observations. Deeper X-ray observations are needed before any conclusions can be reached regarding this particular object.

J355.91977+00.34170

The lack of X-ray detection at this position may be attributed to the peculiar environment that the cluster resides. This cluster is at $z_{spec}=0.261$ (GMBCG

Table 4
X-Ray Spectral Fitting Results

GMBCG Catalog Name	<i>Chandra</i> ObsID	Reduced χ^2	Mass Deposition Rate (M_\odot/yr)	Mass Deposition Rate Excluding 2kpc (M_\odot/yr)	SFR_{LIR} (M_\odot/yr)
W4BCG-R					
J027.58864-10.09181	11711	1.6	105.1 [†]	126.9 [†]	215.9 ⁺¹⁷⁸ ₋₁₂₅
J125.25942+07.86314	1647	1.8	23.5±4.7	22.8±4.7	102.8 ⁺²⁴ ₋₇₆
–	17194	1.9	23.0±3.8	20.4±3.7	102.8 ⁺²⁴ ₋₇₆
–	17563	2.5	30.0±3.4	27.9±3.4	102.8 ⁺²⁴ ₋₇₆
J128.72875+55.57253	1645	1.7	20.0 [†]	19.1 [†]	43.3 ^{+18.9} ₋₄
–	4940	4.0	17.8±8.3	24.0±6.8	43.3 ^{+18.9} ₋₄
J160.18541+39.95313	1652	3.6	36.7±5.3	37.4±5.2	118.7 ⁺¹³⁷ ₋₃₈
W4BCG-P					
J132.60301+37.78597	11576	1.7	106.0±23.5	53.4±23.9	39.7 ⁺⁶⁶ ₋₁₄
J133.71068+62.31389	16138	1.1	183.1±56.3	149.2±56.9	157.4 ⁺²⁷ ₋₇₀
J140.28593+45.64928	827	1.8	– [‡]	2.2 [†]	135.9 ⁺²⁰ ₋₆₀

[†] These fitting results represent maximum values based upon 95% confidence.

[‡] Fitting approached zero or null value.

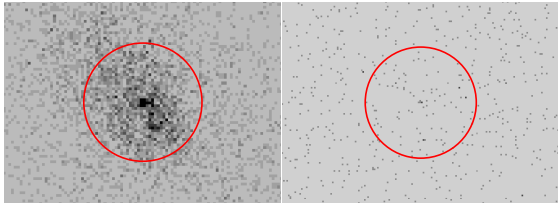


Figure 10. The left panel shows J128.72875+55.57253 detected in the *Chandra* data with an exposure time of 9 ks and $z_{spec} = 0.24118$, while the right panel shows J125.63314+05.95189 not detected in the *Chandra* data with an exposure time of 8 ks and $z_{spec} = 0.081474$. The circles are centered on the reported SDSS positions and are 40 kpc in size.

gives $z_{ph}=0.23$), and it is merging with a nearby cluster at $z_{spec}=0.267$ ($z_{ph}=0.27$ from GMBCG) that is 5.4' away. The entire system is usually referred to as ZwCl 2341.1+0000, whose ICM is known to be disturbed and elongated in shape (van Weeren et al. 2009). While there is X-ray emission from the whole structure, the peak lies in between the two clusters and hence is offset from either BCGs. Under this circumstance, it might not be applicable to discuss the existence of a CC cluster.

J125.63314+05.95189

While the *Chandra* exposure at this position is only 8 ks, the short integration probably is not the reason for the non-detection because the object is very nearby ($z_{spec}=0.0815^3$). In Fig. 10, we show that for another W4BCG with a similar exposure time yet higher redshift, there is still a clear X-ray detection. We do note that this particular W4BCG is identified as being in a low-richness or “poor” cluster.

Due to the small sample and the aforementioned complications, we conclude that deeper X-ray observations of more W4BCGs are needed in order to put the connection of starforming BCGs and cool-core clusters on a more solid ground.

³ This BCG is at $z_{spec}=0.0815$ based on the SDSS DR7, however GMBCG accidentally does not use this value and keeps quoting $z_{ph}=0.132$ instead. Nevertheless, we verify that it indeed belongs to a cluster at $z=0.08$. It is surrounded by ~ 12 red galaxies at $z_{ph}=0.08 \pm 0.02$ that form a clear red sequence, and it is the brightest among all potential members.

6. DISCUSSION

While the common wisdom about BCGs at low redshifts is that they are quiescent galaxies, we have shown that the W4BCGs presented here are exceptions. In most cases, their W4 emissions are due to dust heated by strong star formation. Admittedly, such exceptions will not change the overall picture of BCGs because they are only a minority (W4BCGs accounting only $\sim 0.8\%$ among the entire GMBCG catalog). However, it is important to understand why such exceptions can happen, because this can be related to the critical question in understanding the evolution of high-mass galaxies, namely, why most high-mass galaxies have their star formation processes quenched early in time.

We first note that the W4BCGs do not seem to have unusual environments. While it is widely believed that mergers could induce star formation, the W4BCGs are not predominantly mergers (see §4.2). Second, as compared to the non-W4BCGs, the W4BCGs as a whole have slightly less stellar mass and some of them can have younger ages. However, these differences are not significant and might be the results of the fitting model degeneracy rather than being real.

Third, the cooling-flow interpretation can only explain a small fraction of W4BCGs. Among ten of them that have archival X-ray data, only seven are detected. While these seven X-ray-detected W4BCGs are consistent with being residing in cool-core clusters, five of them have their mass deposition rates (from a cooling flow model) less than their inferred SFRs.

Therefore, our investigations thus far still do not seem to be leading to a universal mechanism that can explain why W4BCGs have high SFRs. Nevertheless, there might be one clue, which is in the redshift distribution of the W4BCGs (see Fig. 2). The high-redshift end ($z \gtrsim 0.4$) of this distribution follows that of the full GMBCG sample, which is not surprising. However, it stays relatively constant at lower redshifts, which is a feature not seen in the redshift distribution of the parent GMBCG sample. While it is still unclear how such a difference can be related to the existence of W4BCGs, it will be worth further study in the future.

7. CONCLUSION

In this paper, we present our systematic census of BCGs at low redshifts ($z < 0.55$) that are still actively forming stars⁴. We use the SDSS-based GMBCG catalog, which is the largest BCG catalog to date, and identify those that have strong mid-IR emissions by their prominent detections in the W4-band (22 μm) in the WISE all-sky survey. The full catalog of these W4BCGs is presented in Table 5, including their various properties as discussed in previous sections.

While some of the W4BCGs could be AGN hosts, the majority of them are not. Therefore, their strong W4 emissions should be powered by dust heating from star formation. Even for those that are possible AGN hosts, we show that their W4 emissions are still most likely due to star formation. Our W4BCGs have median SFR of $\sim 50 M_{\odot}/\text{yr}$, and some have SFR as high as 500–1000 M_{\odot}/yr . Clearly, the W4BCGs are quite contrary to what is expected for BCGs at low redshifts, which are believed to be old, passively evolving galaxies (i.e., “red-and-dead”). There have been a number of studies reporting some low-redshift BCGs that still have non-negligible star formation, but their SFRs are lower than what we observe among these W4BCGs and/or have smaller sample sizes. Although such actively star-forming BCGs are only a minority among all BCGs, their very existence could have important implications to the evolution of very high mass galaxies.

Our investigations so far are not able to answer why these BCGs are still actively forming stars at such a late stage. The previous studies of low-redshift BCGs that are still not completely “dead” usually attribute the star formation triggering mechanism to the cooling flows in cool-core clusters. However, for the seven identified to be in cool-core clusters based upon X-ray data, the possible mass deposition rates due to a cooling flow fall significantly short to explain the observed SFRs, and thus the true triggering mechanism still remains a mystery. One possible clue to solve this problem could be that W4BCGs are different from the quiescent majority in their redshift distribution: their number is redshift independent as compared to the whole GMBCG sample. Further study of field galaxies will be necessary to shed new light to the understanding of this behavior.

We acknowledge the support of NASA’s Astrophysics Data Analysis Program under grant number NNX15AM92G. This publication makes use of data products from the Wide-field Infrared Survey Explorer, which is a joint project of the University of California, Los Angeles, and the Jet Propulsion Laboratory/California Institute of Technology, funded by the National Aeronautics and Space Administration. We would also like to thank Zhiyuan Ma for his help with

⁴ During the revision of this paper, Bonavenutra et al. (2017) posted their paper on the study of star-forming BCGs, with the same main title as ours. The majority ($\sim 75\%$) of the star-forming BCGs in their sample, however, are at $z > 0.55$ and thus are beyond the redshift range of our W4BCGs. In this sense, the high SFRs observed in the W4BCGs are more difficult to understand because they are supposed to settle down already at such a late time of the universe.

HIPE.

REFERENCES

- Arnaud, K. A. 1996, in Jacoby G. H., Barnes J., eds, ASP Conf. Ser. Vol. 101, *Astronomical Data Analysis Software and Systems V*. Astron. Soc. Pac., San Francisco, p. 17
- Arnouts, S., Cristiani, S., Moscardini, L., et al. 1999, *MNRAS*, 310
- Assef, R. J., Stern, D., Kochanek, C. S., et al. 2013, *ApJ*, 772
- Baldwin, J. A., Phillips, M. M., & Terlevich, R. 1981, *PASP*, 93
- Brinchmann, J. o. 2004, *MNRAS*, 351
- Bruzual, G., & Charlot, S. 2003, *MNRAS*, 344
- Calzetti, D. 2001, *PASP*, 113
- Chabrier, G. 2003, *PASP*, 115
- Chary, R., & Elbaz, D. 2001, *ApJ*, 556
- Chen, Y., et al. 2007, *A&A*, 466
- Cowie, L. L., Songaila, A., Hu, E. M., Cohen, J. G., et al. 1996, *AJ*, 112
- Dale, D., & Helou, G. 2002, *ApJ*, 576
- Dale, D. A., Helou, G., et al. 2014, *ApJ*, 784
- De Lucia, G., et al. 2006, *MNRAS*, 366
- Donahue, M., et al. 2015, *ApJ*, 805
- Dubinski. 1998, *ApJ*, 502
- Eales, S., et al. 2010, *PASP*, 122
- Elbaz, D., et al. 2010, *A&A*, 518
- . 2011, *A&A*, 533
- Fabian, A. C., & Nulsen, P. E. J. 1977, *MNRAS*, 180
- Fogarty, K., et al. 2015, *ApJ*, 813
- Fruscione, A., et al. 2006, *SPIE*, 6270
- Griffin, M. J., et al. 2010, *A&A*, 518
- Hao, J., McKay, T. A., Koester, B. P., et al. 2010, *ApJS*, 191
- Hudson, D. S., Mittal, R., Reiprich, T. H., et al. 2010, *A&A*, 513
- Ilbert, O., Arnouts, S., McCracken, H. J., et al. 2006, *A&A*, 457
- Jarrett, T. H., Cohen, M., et al. 2011, *ApJ*, 735
- Kaastra, J. 1992, *An X-Ray Spectral Code for Optically Thin Plasmas* (Internal SRONLeiden Report, updated version 2.0)
- Kalberla, P. M. W., Burton, W. B., Hartmann, D., et al. 2005, *A&A*, 440
- Kauffmann, G., Heckman, T. M., Tremonti, C., et al. 2003a, *MNRAS*, 346
- Kauffmann, G., et al. 2003b, *MNRAS*, 341
- Kennicutt, R. C. 1998, *ARAA*, 36
- Kewley, L. J., Dopita, M. A., Sutherland, R. S., et al. 2001, *ApJ*, 556
- Lang, D. 2014, *AJ*, 147
- Lang, D., Hogg, D. W., & Schlegel, D. J. 2014, *Arxiv e-print*
- Liedahl, D. A., Osterheld, A. L., & Goldstein, W. H. 1995, *ApJ*, 438
- Ma, Z., & Yan, H. 2015, *ApJ*, 811
- Magnelii, B., Elbaz, D., Chary, R., et al. 2009, *A&A*, 496
- Mateos, S., Alonso-Herrero, A., Carrera, F. J., et al. 2012, *MNRAS*, 426
- McDonald, M., Bayliss, M., Benson, B. A., et al. 2012, *Nature*, 488
- McDonald, M., et al. 2016, *ApJ*, 817
- Mewe, R., Gronenschild, E. H. B. M., & van den Oord, G. H. J. 1985, *A&A*, 62
- Mewe, R., Lemen, J. R., & van den Oord, G. H. J. 1986, *A&A*, 65
- Mittal, R., et al. 2017, *MNRAS*, 465
- Molendi, S., & Pizzolato, F. 2001, *ApJ*, 560
- Molendi, S., Tozzi, P., et al. 2016, *A&A*, 595
- Mushotzky, R. F., & Szymkowiak, A. E. a. 1988, in *NATO ASIC Proc. 229: Cooling Flows in Clusters and Galaxies*, ed. A. C. Fabian, 53-62
- O’Dea, C., et al. 2005, *ApJ*, 681
- Oliver, S., Bock, J., et al. 2012, *MNRAS*, 424
- Ott, S. 2010, in *ASP Conf. Ser. 434, Astronomical Data Analysis Software and Systems XIX*, ed. Y. Mizumoto, K.-I. Morita, and M. Ohishi (San Francisco, CA: ASP), 139
- Pilbratt, G. L., et al. 2010, *A&A*, 518
- Roseboom, I. G., et al. 2010, *MNRAS*, 409
- Rykoff, E. S., et al. 2014, *ApJ*, 785
- Salpeter, E. E. 1955, *ApJ*, 121
- Santos, J. S., Rosati, P., Tozzi, P., et al. 2008, *A&A*, 483

- Santos, J. S., Tozzi, P., Rosati, P., & Böhringer, H. 2010, *A&A*, 521
- Siebenmorgen, & Krügel. 2007, *AA*, 462
- Smith, A. J., et al. 2012, *MNRAS*, 419
- Stern, D., Assef, R. J., Benford, D. J., et al. 2012, *ApJ*, 753
- Tozzi, P., Gastaldello, F., et al. 2015, *A&A*, 580
- Tremonti, C. A., et al. 2004, *ApJ*, 613
- Valiante, E., et al. 2016, *MNRAS*, 462
- van Weeren, R. J., et al. 2009, *A&A*, 506
- Viero, M. P., et al. 2013, *ApJ*, 772
- . 2014, *ApJS*, 210
- Vikhlinin, A., Burenin, R., Forman, W. R., et al. 2007, in *Heating versus Cooling in Galaxies and Clusters of Galaxies*, ed. H. Böhringer, G. W. Pratt, A. Finoguenov, & P. Schuecker , 48
- Wang, L., et al. 2014, *MNRAS*, 444
- Wright, E. L., Eisenhardt, P. R. M., et al. 2010, *ApJ*, 140
- York, D. G., Adelman, J., et al. 2000, *AJ*, 120

APPENDIX
W4BCGS IN REDMAPPER

While we focused on the GMBCG catalog for our search of W4BCGs, the same procedure can be applied to other cluster catalogs. One such catalog is that produced by the redMaPPer algorithm (Rykoff et al. 2014). Like the GMBCG catalog, the redMaPPer catalog was produced by the use of a cluster finding algorithm on SDSS data. However, redMaPPer utilized SDSS DR8 photometric data and different criteria for cluster identification. The redMaPPer catalog consists of 26,111 cluster candidates covering a redshift range of $0.08 < z < 0.55$, roughly half the size of the GMBCG catalog despite covering a larger area and similar redshift range. To check for possible overlap between the two, we cross-matched the catalogs using a radius of $400''$, which corresponds to ~ 2 Mpc at the median redshift $z = 0.35$. There is a possible overlap of 14,386 cluster candidates between the redMaPPer and GMBCG catalog.

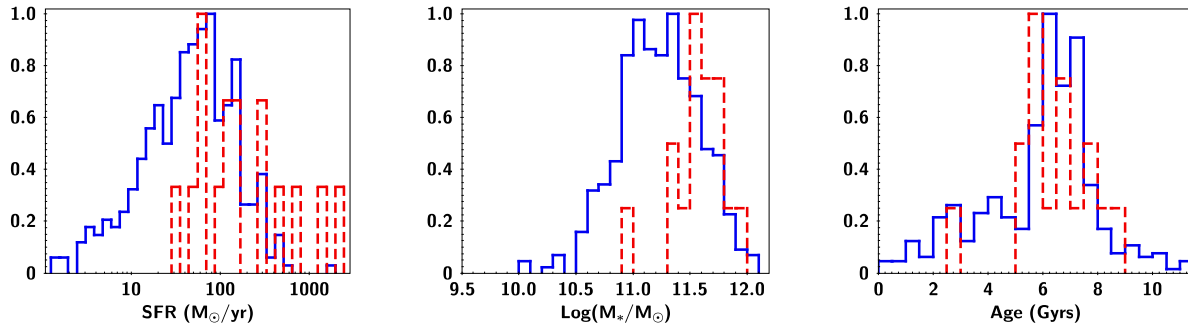


Figure 11. Comparison of the derived SFR (left), stellar mass (middle), and age (right) for the W4BCGs from the GMBCG catalog (solid blue) and the redMaPPer catalog (red dashed), following the same SED fitting procedure as in §4.3. The fit to the stellar population is based on E(B-V) up to 0.3 mag. Each graph is normalized for easy comparison.

Following the same procedure outlined in §3, we searched for BCGs in the redMaPPer catalog that had secure W4 detections. The final sample of W4BCGs in the redMaPPer consists of 16 candidates ($\sim 0.07\%$ of the total catalog). We performed the same SED analysis for these objects following the procedures in §4.3. Their L_{IR} -based SFR, as well as the stellar mass and the age of their stellar populations, are shown in the histograms in Fig. 11. For comparison, we also plot the distributions of the W4BCGs from the GMBCG catalog. Despite the small number of sources, it seems that redMaPPer W4BCGs have slightly higher masses and SFRs as compared to the GMBCG sample. However, the fact remains that these W4BCGs exhibit a high amount of star formation based upon their L_{IR} .

Table 5
Photometry and Derived Properties for W4BCGs

GMBCG Catalog Name	RA(J2000) [†]	DEC(J2000) [†]	z_{phot}^{\dagger}	z_{spec}^{\dagger}	Richness [†]	u	g	r	i	z	W1	W2	W3	W4	$Log(L_{IR}/L_{\odot})$	SFR(M _⊙ /yr)	Age(Gyr)	$Log(M^*/M_{\odot})$	AGN
GMBCG 3000.12121+15.71478	0.12121387	15.71477557	0.11±0.03	0.115441	8	19.42±0.07	17.48±0.01	16.48±0.0	15.98±0	15.61±0.01	15.59±0	15.98±0.01	15.3±0.06	14.49±0.19	10.94 ^{+0.37} _{-0.37}	8.71 ^{+8.19} _{-9.7}	7.4 ^{+3.49} _{-3.49}	10.94 ^{+0.14} _{-0.06}	BPT
GMBCG 3001.48978+15.69867	1.48977991	15.69867485	0.24±0.02	0.218624	10	21.13±0.34	18.88±0.02	17.44±0.01	16.87±0.01	16.49±0.02	16.33±0.01	16.48±0.01	15.57±0.08	14.63±0.2	11.56 ^{+0.27} _{-0.27}	36.4 ^{+31.58} _{-21.86}	7.5 ^{+1.12} _{-1.12}	11.5 ^{+0.69} _{-0.69}	BPT
GMBCG 3002.18580+00.08110	2.1857999	0.08110011	0.38±0.04	0.0	10	21.5±0.55	20.54±0.07	18.87±0.02	18.31±0.02	17.73±0.02	16.59±0.01	16.34±0.01	14.97±0.06	13.82±0.12	12.43 ^{+0.25} _{-0.25}	266.44 ^{+211.86} _{-139.39}	6.57 ^{+1.74} _{-1.74}	11.07 ^{+0.61} _{-0.61}	WISE
GMBCG 3002.89046+15.21398	2.89045783	15.21398079	0.3±0.03	0.0	9	19.98±0.1	19.23±0.02	18.39±0.01	18.09±0.01	17.65±0.04	16.29±0	15.85±0.01	14.96±0.04	14.74±0.21	12.39 ^{+0.07} _{-0.07}	247.17 ^{+45.65} _{-31.79}	1.67 ^{+0.14} _{-0.14}	10.74 ^{+0.66} _{-0.66}	WISE
GMBCG 3007.75699-09.61500	7.75699533	-9.61499813	0.16±0.04	0.0	8	20.84±0.28	19.21±0.02	18.13±0.01	17.48±0.01	17.07±0.04	16.87±0.01	17.40±0.01	14.64±0.03	13.25±0.06	11.72 ^{+0.27} _{-0.27}	51.96 ^{+4.4} _{-3.99}	8.86 ^{+2.22} _{-2.22}	11.05 ^{+0.08} _{-0.08}	NONE
GMBCG 3011.86695-00.60513	11.86695358	-0.60513368	0.42±0.02	0.429752	10	22.35±1.09	20.66±0.08	18.84±0.02	18.11±0.02	17.74±0.05	17.27±0.02	17.36±0.04	15.7±1.26	13.92±0.15	12.01 ^{+0.41} _{-0.41}	125.63 ^{+139.36} _{-84.47}	6.45 ^{+1.78} _{-1.78}	11.64 ^{+0.07} _{-0.11}	NONE
GMBCG 3015.05143+14.84481	14.84481029	14.84481029	0.38±0.07	0.0	8	21.27±0.3	20.81±0.05	19.35±0.02	18.72±0.02	18.2±0.05	16.98±0.01	16.74±0.01	15.8±0.08	14.72±0.17	12.06 ^{+0.26} _{-0.26}	112.74 ^{+137.40} _{-69.92}	7.12 ^{+0.25} _{-0.25}	11.53 ^{+0.09} _{-0.09}	WISE
GMBCG 3027.06772+00.32915	27.06772378	0.32915166	0.15±0.02	0.0918369	11	18.16±0.03	16.72±0	15.86±0	15.43±0	15.17±0.01	15.09±0	15.27±0	14.81±0.03	14.04±0.09	10.85 ^{+0.35} _{-0.35}	7.067 ^{+7.52} _{-3.92}	6.5 ^{+0.92} _{-0.92}	11.22 ^{+0.06} _{-0.06}	NONE
GMBCG 3027.24559-00.70620	27.24558949	-0.7062	0.35±0.02	0.0	14	22.49±0.7	20.65±0.04	18.93±0.02	18.31±0.01	17.93±0.03	17.28±0.01	17.74±0.03	18.24±0.6	14.38±0.11	11.39 ^{+0.16} _{-0.16}	24.6 ^{+3.92} _{-7.75}	6.32 ^{+0.36} _{-0.36}	11.36 ^{+0.07} _{-0.07}	NONE
GMBCG 3027.28864-10.09181	27.28863802	-10.09180529	0.31±0.08	0.365	16	19.57±0.18	18.49±0.03	17.16±0.01	16.62±0.01	16.14±0.03	15.61±0	16.03±0.01	15.01±0.05	14.0±0.12	12.33 ^{+0.27} _{-0.27}	215.92 ^{+124.74} _{-73.74}	6.98 ^{+1.3} _{-1.3}	12.05 ^{+0.1} _{-0.1}	BPT
GMBCG 3027.86875+14.38572	27.86875171	14.38572344	0.35±0.1	0.0	9	22.07±0.28	21.15±0.06	19.86±0.03	19.23±0.03	18.94±0.06	17.9±0.02	17.97±0.04	16.24±0.09	15.0±0.19	11.83 ^{+0.34} _{-0.34}	67.33 ^{+36.6} _{-26.68}	6.38 ^{+2.09} _{-2.09}	11.0±0.1	WISE
GMBCG 3029.17012-00.37641	29.17012063	-0.37640939	0.36±0.09	0.0	12	21.34±0.29	20.63±0.06	19.48±0.04	18.96±0.03	18.51±0.07	17.78±0.02	17.49±0.03	15.9±0.07	14.65±0.15	12.01 ^{+0.35} _{-0.35}	103.04 ^{+56.68} _{-36.8}	6.08 ^{+1.31} _{-1.31}	11.08 ^{+0.11} _{-0.11}	NONE
GMBCG 3029.56746+00.00350	29.56746057	0.00349558	0.42±0.02	0.0	20	23.48±1.2	21.99±0.12	20.26±0.04	19.54±0.03	19.09±0.09	18.35±0.03	18.84±0.09	18.51±0.71	15.01±0.19	11.4 ^{+0.18} _{-0.18}	25.04 ^{+4.49} _{-3.54}	6.17 ^{+2.63} _{-2.63}	11.09 ^{+0.14} _{-0.14}	NONE
GMBCG 3029.97041-08.20800	29.97040719	-8.20800187	0.34±0.03	0.346697	9	22.8±1.55	20.29±0.05	18.63±0.02	18±0.02	17.51±0.05	17.0±0.1	17.35±0.03	-99±99	14.59±0.16	11.9 ^{+0.35} _{-0.35}	79.67 ^{+104.11} _{-36.88}	6.99 ^{+1.74} _{-1.74}	11.52 ^{+0.09} _{-0.09}	NONE
GMBCG 3034.05742-00.72531	34.05742358	-0.72531111	0.31±0.07	0.0	15	19.91±0.14	19.12±0.02	18±0.01	17.55±0.01	17.14±0.03	16.85±0.01	16.93±0.02	15.97±0.07	15.07±0.2	11.79 ^{+0.26} _{-0.26}	61.12 ^{+35.67} _{-26.8}	6.44 ^{+2.05} _{-2.05}	11.3 ^{+0.84} _{-0.84}	NONE
GMBCG 3038.44672-08.84924	38.44672304	-8.84923564	0.28±0.02	0.0	18	22.23±1.77	19.02±0.03	17.5±0.01	16.96±0.01	16.48±0.03	16.36±0.01	16.77±0.02	18.2±0.74	14.83±0.2	11.12 ^{+0.43} _{-0.43}	13.33 ^{+23.17} _{-13.51}	7.58 ^{+1.82} _{-1.82}	11.75 ^{+0.08} _{-0.08}	NONE
GMBCG 3039.77836-07.69936	39.77836437	-7.69935863	0.39±0.07	0.0	9	25.05±2.79	20.98±0.09	19.68±0.05	18.9±0.04	18.48±0.09	17.76±0.02	18.09±0.05	16.36±0.09	15.1±0.19	11.88 ^{+0.29} _{-0.29}	75.16 ^{+71.7} _{-43.54}	6.49 ^{+1.79} _{-1.79}	11.28±0.1	NONE
GMBCG 3044.83916+00.30161	44.83916234	0.30160525	0.14±0.02	0.1380	13	17.77±0.09	17.56±0.01	16.82±0.01	16.45±0.01	16.15±0.02	16.25±0.01	16.58±0.02	14.87±0.03	14.59±0.17	11.5 ^{+0.11} _{-0.11}	31.91 ^{+9.04} _{-6.27}	5.11 ^{+0.71} _{-0.71}	10.81±0.16	NONE
GMBCG 3048.94591-07.99395	48.94590677	-7.99395007	0.24±0.07	0.274238	12	17.47±0.1	18.45±0.01	17.54±0.01	17.2±0.01	16.84±0.03	16.39±0	16.17±0.01	14.64±0.02	14.15±0.12	12.43 ^{+0.04} _{-0.04}	273.3 ^{+283.93} _{-65.98}	2.35 ^{+0.99} _{-0.99}	11.07 ^{+0.09} _{-0.09}	BOTH
GMBCG 3055.26483-05.56434	55.26483489	-5.56434196	0.45±0.05	0.0	9	22.76±0.82	21.49±0.09	19.93±0.04	19.21±0.03	18.51±0.06	16.06±0	15.52±0	14.81±0.04	13.87±0.1	11.87 ^{+0.23} _{-0.23}	493.4 ^{+511.68} _{-286.82}	1.28 ^{+0.96} _{-0.96}	11.71 ^{+0.09} _{-0.09}	WISE
GMBCG 3112.54887-42.00126	112.54886592	-42.00126089	0.41±0.07	0.0	12	21.46±0.3	20.77±0.05	19.93±0.04	19.37±0.03	18.94±0.08	17.72±0.02	17.89±0.04	16.75±0.2	14.58±0.18	11.74 ^{+0.11} _{-0.11}	55.39 ^{+57.41} _{-20.73}	5.53 ^{+1.25} _{-1.25}	11.06 ^{+0.09} _{-0.09}	NONE
GMBCG 3113.43436+38.87798	113.43436575	38.87798154	0.18±0.02	0.0	9	20.48±0.18	18.73±0.02	17.6±0.01	17.09±0.01	16.76±0.02	16.75±0.01	16.76±0.02	14.9±0.04	13.92±0.09	11.86 ^{+0.53} _{-0.53}	77.2 ^{+51.53} _{-16.13}	6.6 ^{+1.77} _{-1.77}	10.67±0.27	BPT
GMBCG 3114.20870+39.33200	114.2086979	39.33200399	0.18±0.03	0.116268	11	19.09±0.08	17.95±0.01	17.16±0.01	16.73±0.01	16.32±0.02	16.75±0.01	16.66±0.02	14.53±0.03	13.14±0.05	11.44 ^{+0.39} _{-0.39}	84.7 ^{+62.61} _{-26.61}	7.34 ^{+1.97} _{-1.97}	11.63 ^{+0.15} _{-0.15}	BPT
GMBCG 3115.36870+44.40880	115.36869909	44.40880028	0.16±0.02	0.132188	14	18.43±0.06	16.84±0.01	15.83±0	15.38±0	15.07±0.01	15.19±0	15.18±0	13.83±0.02	12.86±0.04	11.93 ^{+0.58} _{-0.58}	62.85 ^{+35.54} _{-23.67}	4.38 ^{+1.85} _{-1.85}	11.11±0.27	BPT
GMBCG 3118.43924+12.64781	118.43924374	12.64780523	0.19±0.03	0.196569	9	17.97±0.07	18.31±0.01	17.27±0.01	16.78±0.01	16.58±0.02	16.36±0.01	16.58±0.02	14.87±0.04	13.55±0.08	11.8 ^{+0.38} _{-0.38}	10.7 ^{+3.67} _{-2.61}	6.97 ^{+0.99} _{-0.99}	11.3±0.03	NONE
GMBCG 3122.41201+34.92700	122.412007888163	34.9270038726458	0.17±0.04	0.0825257	15	17.59±0.01	16.47±0	15.63±0.01	15.23±0	14.9±0	14.87±0	15.17±0	15.12±0.05	14.39±0.15	10.41 ^{+0.21} _{-0.21}	2.59 ^{+4.99} _{-0.99}	6.31 ^{+0.48} _{-0.48}	11.4±0.03	NONE
GMBCG 3122.51706+41.27283	122.517057625448	41.2728302106215	0.2±0.04	0.133547	10	17.5±0.03	17.47±0	16.49±0.01	16.09±0	15.76±0.01	15.71±0	16.23±0.01	16.27±0.13	14.26±0.13	10.75 ^{+0.19} _{-0.19}	5.61 ^{+0.97} _{-0.97}	8.27 ^{+0.81} _{-0.81}	11.3±0.03	NONE
GMBCG 3123.72723+07.08626	123.72726566836	7.08622106604503	0.12±0.03	0.0	10	18.02±0.02	16.97±0.01	16.41±0	16.02±0.01	15.85±0.01	15.74±0	15.98±0.01	13.71±0.01	13.19±0.06	11.79 ^{+0.49} _{-0.49}	61.8 ^{+14.83} _{-9.32}	2.28 ^{+0.45} _{-0.45}	10.37±0.07	NONE
GMBCG 3124.12529+34.58306	124.125285691121	34.5830535582585	0.42±0.1	0.0	10	22.4±0.28	20.43±0.06	19.21±0.03	18.56±0.02	18.27±0.06	17.79±0.02	18.04±0.05	16.69±0.18	14.61±0.17	11.79 ^{+0.42} _{-0.42}	61.83 ^{+99.12} _{-51.17}	7.74 ^{+1.47} _{-1.47}	11.29±0.08	NONE
GMBCG 3125.03628+05.76234	125.036284701265	5.7623636006056	0.12±0.03	0.0807631	6	17.41±0.02	16.12±0	15.39±0	14.95±0	14.69±0	14.49±0	14.79±0	12.6±0	11.73±0.01	11.3 ^{+0.03} _{-0.03}	19.94 ^{+1.29} _{-1.29}	5.76 ^{+2.18} _{-2.18}	11.01±0.05	NONE
GMBCG 3125.29542+07.86144	125.29542811613	7.86313797474906	0.14±0.02	0.0	24	17.98±0.03	16.71±0	15.94±0	15.48±0	15.23±0.01	15.05±0	15.44±0.01	13.83±0.02	12.8±0.04	12.01 ^{+0.09} _{-0.09}	102.85 ^{+23.57} _{-15.82}	6.02 ^{+0.78} _{-0.78}	11.24±0.15	NONE
GMBCG 3125.33837+16.12444	125.338367115871	16.1244733982432	0.12±0.02	0.126844	8	19.01±0.05	17.79±0.01	17.1±0.01	16.74±0.01	16.46±0.01	16.47±0.01	16.84±0.02	14.88±0.04	14.16±0.13	11.34 ^{+0.24} _{-0.24}	22.05 ^{+16.4} _{-13.66}	3.87 ^{+0.81} _{-0.81}	10.55±0.06	NONE
GMBCG 3126.54276+15.86042	126.542762757289	15.860477369936	0.19±0.03	0.0	13	18.5±0.03	18.4±0.01	17.64±0.01	17.12±0.01	17.40±0.01	16.41±0.01	16.32±0.01	15.36±0.06	14.32±0.15	11.55 ^{+0.42} _{-0.42}	35.3 ^{+28.66} _{-13.66}	8.81 ^{+1.36} _{-1.36}	11.06±0.04	NONE
GMBCG 3126.74500+53.21243	126.744995027599	53.2124287052539	0.11±0.01	0.117597															